

1 Revision 3: Experimental formation of pyroxenite veins by reactions  
2 between olivine and Si, Al, Ca, Na and Cl-rich fluids at 800 °C and 800  
3 MPa; implications for fluid metasomatism in the mantle wedge.

4  
5 Thomas B. Grant<sup>1,2</sup>, Daniel E. Harlov<sup>1</sup>, Dieter Rhede<sup>1</sup>

6  
7 <sup>1</sup>Deutsches GeoForschungsZentrum

8 Telegrafenberg

9 D-14473 Potsdam

10 FR Germany

11

12 <sup>2</sup> Department of geology and mineral resources engineering,

13 Norwegian University of Science and Technology (NTNU)

14 7491 Trondheim, Norway

15

16 **ABSTRACT**

17 Fluids buffered by a plagioclase matrix are experimentally reacted with olivine  
18 megacrysts at 800 °C and 800 MPa (piston cylinder press, CaF<sub>2</sub> assembly) to form  
19 secondary veins of orthopyroxene ± clinopyroxene in the olivine. Fluids utilized were  
20 varied in both amount (0 – 2 wt.%) and salinity (0 – 8M NaCl). Assuming equilibrium  
21 with the plagioclase matrix, they are presumed enriched in Si, Al, Ca, Na, and Cl and  
22 are thereby similar in composition to slab derived fluids. The experiments provide  
23 controlled, multicomponent analogues of Si-metasomatism in the mantle wedge  
24 above subduction zones. The veins are dominated by orthopyroxene with minor  
25 clinopyroxene and form complex interconnected networks along fractures in the  
26 olivine. The reaction is rate limited by interfacial process of dissolution and

27 precipitation. Porosity is developed throughout the veins and along sub grain  
28 boundaries in the olivine megacrysts. These veins strongly resemble the textures  
29 observed in secondary metasomatic orthopyroxene veins widely reported in upper  
30 mantle xenoliths within arc magmas. A review of literature data on natural samples  
31 and experiments suggests that orthopyroxene ± clinopyroxene veins primarily form  
32 between 750 – 950 °C and over a large pressure range from 0.8 – 3.4 GPa. The  
33 abundance and composition of these metasomatic veins may vary as a function of  
34 pressure, variances in the fluid-rock partition coefficients, and/or by modification of  
35 the metasomatic fluid during the reaction.

36

37

## 38 INTRODUCTION

39 During partial melting or dehydration of subducting oceanic lithosphere, Si-rich melts  
40 (Schiano et al., 1995; Prouteau et al., 2001), aqueous fluids (Manning, 2004), or  
41 supercritical liquids (Hermann et al., 2006) are released into the overlying mantle  
42 wedge. This leads to Si metasomatism in the mantle wedge by the consumption of  
43 olivine and the precipitation of secondary orthopyroxene (as well as other phases).  
44 This form of metasomatism can be most simply expressed by the following  
45 relationship:  $(\text{Mg,Fe})_2\text{SiO}_4 + \text{SiO}_2 = 2(\text{Mg,Fe})\text{SiO}_3$ . Metasomatic orthopyroxene,  
46 formed by infiltrating Si rich melts or fluids in the sub arc mantle, have been observed  
47 in mantle xenoliths within arc lavas (Smith and Riter; 1997; Smith et al., 1999;  
48 Grégoire et al., 2001; McInnes et al., 2001; Franz et al., 2002; Arai et al., 2003; Arai  
49 et al. 2004; Downes et al., 2004; Bell et al., 2005; Berly et al., 2006; Ishimaru et al.,  
50 2007; Grégoire et al., 2008; Ishimaru and Arai, 2009; Soustelle et al., 2010; Ishimaru  
51 and Arai, 2011; Soustelle et al., 2011) and peridotite complexes (Morishita et al.,

52 2003; Malaspina et al., 2006; Vrijmoed et al., 2013). Experimental studies involving  
53 melts (Rapp et al., 1999; Rapp et al., 2010; Malik et al., 2015) or crystalline quartz +  
54 fluid (Yund et al., 1997; Milke et al., 2009; Milke et al., 2011; Gardés et al., 2012;  
55 Milke et al., 2013) have also shown that olivine will be consumed to form secondary  
56 orthopyroxene.

57 Reactions between slab derived fluids or melts and the mantle wedge have  
58 significant implications for the recycling of elements at subduction zones and the  
59 compositions of arc lavas. It is therefore vital to understand the exchange of major  
60 and trace elements during reactions between Si-rich fluids and olivine dominated  
61 peridotite rocks. For example, how do the compositions of pyroxenite veins vary and  
62 how are metasomatic fluids modified by reactions in the mantle wedge? These  
63 processes are poorly understood (Spandler and Pirard, 2013).

64 In terms of major element chemistry, slab derived fluids are thought to be rich  
65 in Si, Al, Na, K, Ca, and Cl as well as fluid mobile elements such as LILE, Sr and Pb  
66 but poor in Mg and Fe (Manning, 2004; Berly et al., 2006). Due to large similarities  
67 in the trace elements and isotopic signatures of arc magmas and the short time scales  
68 of recycling from oceanic crust, it is thought that slab derived fluids are primarily  
69 transported through the mantle wedge by channelized flow (Zack and John, 2007).  
70 However, pervasive flow of fluids has also been observed (Malaspina et al., 2006),  
71 and it is likely that some pervasive flow may occur perpendicular to the main channel.  
72 In such a scenario the majority of the fluid may pass unmodified for substantial  
73 distances in the mantle wedge, but the peridotite wall rocks become partially modified  
74 by the influx Si-rich fluids. Furthermore, diapiric mélange zones may also bring felsic  
75 material in contact with mafic peridotite rocks (Marschall and Schumacher, 2012).  
76 Exchange of elements between them, via channelized, Si-rich fluids, can result in the

77 formation of vein sequences such as those observed in the Svartberget peridotite,  
78 Norway which shows a series of zones from peridotite to pyroxenite, garnetite and  
79 eclogite towards the country rock migmatite gneiss (for further details see Vrijmoed  
80 et al., 2013).

81         In order to gain further understanding of how these metasomatic processes  
82 proceed in the mantle wedge, a series of experiments have been conducted in which  
83 Si-rich fluids are reacted with olivine megacrysts in a plagioclase matrix to form  
84 orthopyroxene and clinopyroxene veins within the olivine megacrysts at conditions  
85 applicable to the lower crust and upper mantle (800 °C and 0.8 GPa). These  
86 experiments expand on a set of simpler experiments involving the reaction between  
87 olivine and quartz  $\pm$  H<sub>2</sub>O to form secondary orthopyroxene (Yund et al., 1997; Milke  
88 et al., 2009; Milke et al., 2011; Gardés et al., 2012; Milke et al., 2013). As slab  
89 derived aqueous fluids are typically rich in Si, Al, Na, K, and Ca and low in Mg and  
90 Fe (Manning, 2004), to a broad extent the use of anorthite-albite plagioclase as a  
91 buffer for the fluids in these experiments is an appropriate analogue for complex  
92 natural metasomatic fluids in the sub arc mantle. Variable amounts of fluid (0–2  
93 wt.%) and variable fluid compositions (pure H<sub>2</sub>O; 2M NaCl and 8M NaCl solutions)  
94 are added to test how these parameters affect the vein mineralogy and composition.  
95 This experimental data is then compared with naturally occurring, metasomatically  
96 induced orthopyroxene and clinopyroxene veins in peridotitic mantle xenoliths. For  
97 these same samples, compositional trends are also explored to see if there are any  
98 potential indicators of fluid evolution, in terms of Mg, Fe, Al, Ca, and Cr, over small  
99 (meter) and long (kilometer) length scales as they pass through the overlying mantle  
100 wedge.

101

102 **ELECTRON PROBE MICRO-ANALYSES (EPMA)**

103 Chemical analyses were taken using a JEOL Hyperprobe JXA-8500F with a field-  
104 emission cathode at the GFZ Potsdam. For olivine, orthopyroxene, and clinopyroxene  
105 operating conditions were 15 kV accelerating voltage and 20  $\mu$ A beam current. For  
106 plagioclase and chlorapatite operating conditions were 10 kV accelerating voltage and  
107 10  $\mu$ A. Silicate, oxide, and metal standards (both synthetic and natural) were used. A  
108 5  $\mu$ m beam diameter was used for plagioclase and chlorapatite analyses whereas beam  
109 sizes of 0 – 1  $\mu$ m were used for olivine, orthopyroxene, and clinopyroxene.

110

111 **EXPERIMENTAL METHODS**

112 All experiments were conducted at the Deutsche GeoForschungsZentrum Potsdam  
113 using Johannes type piston cylinder apparatus (Johannes et al. 1971; Johannes, 1973).  
114 Pressures of 800 MPa, temperatures of 800°C and run durations of 8 days were used.  
115 Seven experiments were conducted in total. In each experiment, the sample charge  
116 consisted of isolated single San Carlos olivine crystal fragments in a plagioclase  
117 matrix (+ minor chlorapatite) with an added fluid component. Added fluid ranged  
118 from 0-2 wt.% (of sample charge) double distilled water and 2 wt.% of either 2 M or  
119 8 M NaCl solution. Compositions of starting materials are given in Table 1 and the  
120 details of the run conditions are given in Table 2.

121 A single crystal of inclusion-free San Carlos olivine was crushed using a metal  
122 pestle and mortar. Crystal fragments with sizes of 250–500 $\mu$ m were separated from  
123 the crushed material using sieves. To prepare the matrix, plagioclase grains were  
124 hand-picked from a sample of partially crushed gabbro from the Bamble Sector, SE  
125 Norway. The plagioclase grains were ground to a fine powder (<50  $\mu$ m) in ethanol

126 using an agate pestle and mortar. This powder consisted of > 96% anorthitic  
127 plagioclase, 2 – 3% chlorapatite and 1 – 2% Cl-rich calcic amphibole.

128 All sample materials were loaded into platinum capsules with dimensions of 1  
129 cm x 3 mm with wall thicknesses of 0.3 mm. The capsules were not pre-saturated  
130 with Fe. A Lampert PUK 3 arc welder was used to seal all capsules at both ends.  
131 Fluids (double distilled water, 2 M or 8 M NaCl solution) were added to the capsule  
132 first via a micro-syringe. The capsules were then half filled with the plagioclase  
133 powder, before several single olivine crystal fragments were added. The remainder of  
134 the capsule was then filled with more plagioclase powder. All capsules were weighed  
135 after the final weld, placed in a 100 °C oven for over an hour, and then weighed  
136 again. No weight loss was observed. In the case of experiment OP001, where no fluid  
137 was added, the plagioclase powder was dried at 100°C for 24 hours before being  
138 added to the capsule.

139 All experiments were conducted in Johannes type piston cylinder apparatus  
140 using CaF<sub>2</sub> pressure media, cylindrical graphite ovens, and Ni/Ni-Cr thermocouples  
141 (Fig. 1). The graphite ovens are expected to buffer the fO<sub>2</sub> of the experiments to  
142 between CCO and CCO-4 (Médard et al. 2008), although the high aH<sub>2</sub>O in the most  
143 hydrous experiments could potentially increase the fO<sub>2</sub> due to dissociation of H<sub>2</sub>O and  
144 H loss through the capsule walls (Botcharnikov et al 2005). The CaF<sub>2</sub> parts were  
145 machined to accommodate four capsules within a single run. Each capsule was  
146 separated by a sheet of biotite. Pressure was initially loaded to ~650 MPa before  
147 heating to 800 °C. The experiment was then raised up to the desired pressure of 800  
148 MPa. Temperature fluctuations were within 1 – 3 °C. After each experiment, the  
149 capsules were cleaned and weighed again. None of the capsules were reduced in  
150 weight, indicating no observable loss of volatiles during the experiment.

151

## 152 **RESULTS**

153 The olivine crystal fragments reacted with the surrounding plagioclase matrix to form  
154 rim coronas of predominantly clinopyroxene and amphibole  $\pm$  phlogopite. In the  
155 olivine grains, vein assemblages of either secondary olivine + clinopyroxene,  
156 clinopyroxene + orthopyroxene, and/or pore trails formed. The veins are the primary  
157 focus of this study.

158

### 159 **Textures**

#### 160 *Pore trails*

161 Small to medium sized pore trails are observed in the olivine grain interiors (Fig. 2;  
162 Fig. 3c-d). Pores range from  $< 1\text{--}2\ \mu\text{m}$  to  $10\text{--}20\ \mu\text{m}$  or greater. Smaller pores have  
163 very round shapes and appear to be closely ( $1\text{--}2\ \mu\text{m}$  apart) and regularly spaced (Fig.  
164 2a). Small pore trails have also been observed along interphase grain boundaries (see  
165 Fig. 3b). Larger pores are much more irregularly shaped (elongate and oblong) and  
166 are more widely spaced (up to tens of  $\mu\text{m}$ ). For examples see Fig. 2b and 3d. Pore  
167 trails tend to not extend completely across the olivine grain and may be curved or  
168 straight forming a complex network (cf. Fig. 2). Similar trails of small fluid inclusions  
169 have been described in olivine from mafic xenoliths (Hansteen et al., 1991),  
170 clinopyroxene in peridotites (Frezzotti et al., 2010), and quartz in granites (Lespinnasse  
171 and Cathelineau, 1990). Open pore spaces have also been observed in sub-arc  
172 xenoliths that have been metasomatised by hydrous fluids (see textures in McInnes et  
173 al., 2001).

174

#### 175 *Secondary olivine patches*

176 Irregular patches and linear veins of secondary olivine, that are richer in Mg  
177 compared to the host olivine, are observed in sample OP002 (cf. Figure 2). The  
178 interface between Mg-rich olivine and primary San Carlos (Mg-poorer olivine) appear  
179 to be slightly diffuse (see Fig. 2b). However, an element line scan indicates that the  
180 Mg-rich olivine, while variable in composition, has a sharp interface with the primary  
181 olivine (Fig. 4). These patches and veins are typically associated with large and small  
182 pores.

183

#### 184 *Pyroxene veins*

185 A complex network of orthopyroxene  $\pm$  clinopyroxene veins, often extending from  
186 the rim to the center or across the whole olivine grain, formed in experiments OP003,  
187 OP004, OP010, and OP016 (Fig. 3d). The thicknesses of the veins vary from several  
188  $\mu\text{m}$  to over 100  $\mu\text{m}$ . The veins are dominated by orthopyroxene with minor  
189 clinopyroxene. Clinopyroxene appears to be more abundant in samples with lower  
190 water contents (OP002 and OP010) or with higher salinity (OP016), however, these  
191 relationships are difficult to quantify. The vein network may include islands of  
192 angular original olivine (Fig. 3d). Contacts between the olivine, orthopyroxene, and  
193 clinopyroxene are compositionally sharp in texture (Fig. (Figs. 4, 5, and 6). Interphase  
194 boundaries between the pyroxene and the olivine are typically lined with small (1–2  
195  $\mu\text{m}$ ) round pores (Fig. 3b), although large pores are also common. Small pores are  
196 also present within the orthopyroxene veins (Fig. 3d).

197 In natural samples, pyroxene typically replaces olivine in the form of (often  
198 thin) pyroxenite veins (e.g., Fig. 2 in Morishita et al., 2003; 2001 Ishimaru et al.,  
199 2007; Ishimaru and Arai, 2011), and along grain boundaries (see Grégoire et al.,  
200 2001; McInnes et al., 2001). Very thin veins, which are typically  $<500 \mu\text{m}$  and as

201 small as ~40–60  $\mu\text{m}$ , of orthopyroxene with complex cross-cutting structures through  
202 olivine grains have also been observed (Soustelle et al., 2011; Bernard and Ionov,  
203 2013). Thin orthopyroxene veins may also contain vesicles (Bernard and Ionov,  
204 2013). Secondary orthopyroxene in natural xenoliths can also form radial aggregates  
205 (Arai et al., 2004; Ishimaru et al., 2007) but these were not observed in our  
206 experiments.

207

## 208 **Mineral chemistry**

### 209 *Secondary olivine*

210 Secondary olivine has an  $X_{\text{Mg}}$  of ~0.97 and is richer in Mg compared to the San  
211 Carlos olivine ( $X_{\text{Mg}}$  ~0.91) (Table 3). The secondary olivine is also depleted in  $\text{Al}_2\text{O}_3$ ,  
212 CaO, and NiO but slightly enriched in  $\text{P}_2\text{O}_5$  and  $\text{SiO}_2$  relative to the San Carlos  
213 olivine. High-Mg secondary olivine in pyroxenites (up to  $X_{\text{Mg}} = 0.97$ ) have been  
214 observed in metasomatised xenoliths from Avacha (Ishimaru and Arai, 2011).

215

### 216 *Orthopyroxene veins*

217 The secondary orthopyroxene veins are Mg rich ( $X_{\text{Mg}} = 0.98\text{--}0.99$ ). In natural  
218 samples, secondary metasomatic orthopyroxene is often characterized by low Al and  
219 Ca (as well as Cr) compared to primary orthopyroxene (Smith and Riter, 1997; Smith  
220 et al., 1999; McInnes et al., 2001; Franz et al., 2002; Arai et al., 2003; Arai et al.,  
221 2004; Downes et al., 2004; Morishita et al., 2003; Berly et al., 2006; Ishimaru et al.,  
222 2007; Grégoire et al., 2008; Ishimaru and Arai, 2011) although there is some  
223 crossover between the two data sets. Secondary orthopyroxene from the experiments  
224 in this study are richer in Al relative to secondary and primary orthopyroxenes from  
225 natural samples (Fig. 7) but have comparable Ca contents to most of the natural data.

226 However, many natural secondary orthopyroxenes have extremely Ca depleted  
227 compositions relative to primary and experimental orthopyroxenes. The  
228 orthopyroxene is also enriched in P<sub>2</sub>O<sub>5</sub> compared to the secondary olivine (see Table  
229 4, and Figs. 5 and 6). This is a rather surprising result as it is well documented that P  
230 preferentially partitions into olivine rather than orthopyroxene over a wide range of P-  
231 T-X and fO<sub>2</sub> conditions (Bishop et al., 1978; Millman-Barris et al., 2008; Mallmann  
232 and O'Neill, 2009; Mallmann et al., 2009; Konzett et al., 2012). It appears that  
233  $D_P^{OPX/fluid}$  is greater than  $D_P^{Ol/fluid}$ . The source of the P is presumably the small  
234 amounts of chlorapatite in the plagioclase matrix.

235 No significant internal zoning patterns were observed within the  
236 orthopyroxene veins. In addition, all elements show sharp step profiles at the interface  
237 between olivine and orthopyroxene (Figs. 5 and 6). The composition of the vein  
238 orthopyroxene also appears to vary with the molar amount of NaCl in the fluid  
239 Increasing molar NaCl in the fluid is correlated with increasing Al<sub>2</sub>O<sub>3</sub> and MnO and  
240 decreasing CaO in the orthopyroxene (Figure 8). In contrast, no strong trends were  
241 observed between the orthopyroxene compositions and the bulk water contents of the  
242 samples.

243 The major elements (MgO, SiO<sub>2</sub>, FeO) have sharp step function profiles when  
244 crossing from olivine to orthopyroxene (Fig 5 and 6). This is also the same for minor  
245 elements within the error of the analyses, e.g. NiO, Al<sub>2</sub>O<sub>3</sub>, CaO. For MnO there is a  
246 near constant composition from olivine to orthopyroxene in Fig 5. In Fig. 6 there is a  
247 trend of increasing MnO across the olivine-orthopyroxene interface. The  
248 concentration of P<sub>2</sub>O<sub>5</sub> increases within the orthopyroxene with increasing distance  
249 from the olivine-orthopyroxene interface. Some scatter in NiO, MnO and P<sub>2</sub>O<sub>5</sub> are  
250 seen within the orthopyroxene veins in Fig 5. In some line scans (not shown) Al<sub>2</sub>O<sub>3</sub>

251 shows symmetrical zoning patterns on either side of the center of the vein, although  
252 this was not a very common feature. In sample OP003, secondary orthopyroxene has  
253 an MnO composition similar to the primary olivine, whereas in in sample OP010  
254 MnO is slightly richer in the orthopyroxene. This was consistent in other line scans of  
255 the same samples.

256

### 257 *Clinopyroxene veins*

258 Two types of Ca-bearing pyroxene were found in the experiments (Table 5). In  
259 sample OP016 (8M NaCl solution) the clinopyroxene is richer in Al<sub>2</sub>O<sub>3</sub>, FeO, MnO,  
260 and Na<sub>2</sub>O compared to the clinopyroxene from samples OP003 and OP010 (pure  
261 H<sub>2</sub>O). Augite/pigeonite was only observed in sample OP010 where it coexists in the  
262 same vein with clinopyroxene. It is higher in Al<sub>2</sub>O<sub>3</sub>, TiO<sub>2</sub>, and Na<sub>2</sub>O but lower in  
263 FeO.

264

## 265 **DISCUSSION**

### 266 **Formation of veins, pore trails and cracks**

#### 267 *Pore trails*

268 Crushing of the San Carlos olivine crystal and loading of pressure onto the sample  
269 during the initial stages of the experiment will introduce micro-fractures into the  
270 olivine grains. These have a structure similar to low angle olivine-olivine grain  
271 boundaries or sub-grain boundaries, i.e. they are planar fractures with a low angle of  
272 mis-orientation that have faster rates of diffusion compared to the adjacent olivine  
273 lattices. Fluid within the experimental charge can then hydrate these fractures during  
274 the experiment. Hydration of grain and interphase boundaries has been demonstrated  
275 in a large number of experimental studies (e.g. Gardés et al. 2012; Milke et al., 2013).

276 Sommer et al. (2008) noted that fluids can become concentrated along dislocation  
277 structures and grain boundaries in olivine. Fluid along fractures in olivine has also  
278 been shown to allow for exchange of H<sub>2</sub>O between melt inclusions and the host  
279 magma (Bakker and Jansen, 1994; Massare et al., 2002; Portnyagin et al., 2008). The  
280 presence of pores in our experiments strongly suggests that a free fluid was present  
281 along the micro-fractures. Inclusion trails in olivine adjacent to secondary  
282 orthopyroxene veins have also been observed by McInnes et al. (2001).

283         Small fluid pores are effective agents for the enhanced dissolution of olivine  
284 and the precipitation of orthopyroxene (Milke et al., 2013; also see the review by  
285 Putnis (2009) for numerous other examples). In systems controlled by grain boundary  
286 diffusion, increasing the fluid to rock ratio significantly enhances the rates of reaction  
287 (Rubie 1986, Gardés et al., 2012; Milke et al., 2013). This is because the diffusion  
288 mechanism changes with increasing hydration of grain boundaries. Diffusion in ‘Dry’  
289 grain boundaries involves breaking of Si-O bonds, which requires high activation  
290 energies. Partially hydrated grain boundaries contain weaker O-H bonds and therefore  
291 the activation energies for diffusion are lower and diffusion rates are higher (Rubie  
292 1986). The development of (interconnected) free-fluid along grain boundaries results  
293 in another change in diffusion mechanism where diffusion rates significantly increase  
294 (Gardés et al., 2012). The development from near dry micro-fractures to partially  
295 hydrated grain boundaries to pores trails shows the various stages of grain boundary  
296 hydration. The pores then become sites of both dissolution of olivine and precipitation  
297 of secondary olivine, orthopyroxene, and clinopyroxene.

298

299 *Secondary olivine*

300 Secondary, Mg-richer olivine was only observed in several samples (OP002) It forms  
301 in locations that are close to or extend from the individual pores or pore tails. The  
302 interface between secondary and primary olivine appears to be sharp ( $< 1 \mu\text{m}$ ) with a  
303 sudden change in major element chemistry. Compositional zoning is then observed in  
304 the secondary olivine. The sharp interface suggests that dissolution and precipitation  
305 are involved in the formation of secondary olivine but that diffusion was not efficient  
306 enough at  $800 \text{ }^\circ\text{C}$  and  $800 \text{ MPa}$  to create a homogenous secondary olivine zone. It is  
307 presumed that secondary olivine in the immediate vicinity of the pore formed first and  
308 that the reaction front moved in a direction perpendicular to the fluid-olivine interface  
309 replacing the primary olivine with secondary olivine. As the length scales increased,  
310 the flux of components across the olivine reaction zone was reduced leading to  
311 diffusion profiles.

312

### 313 *Pyroxene veins*

314 Step function concentration profiles across the olivine-orthopyroxene interfaces and  
315 (generally) flat concentrations profiles across the orthopyroxene veins and within  
316 olivine (Figs, 5 and 6) suggest that the reaction was limited by interfacial processes  
317 (dissolution and precipitation) and not by diffusion. The association of large pores  
318 with the secondary veins strongly suggests that a free fluid phase was involved in the  
319 reaction. Although line scans across orthopyroxene veins in natural samples have not  
320 been reported, the similar textures and the presence of associated fluid inclusions  
321 suggest that pyroxene veins in the upper mantle are also rate limited by fluid mediated  
322 interfacial processes (particularly at lower temperatures).

323 The orthopyroxene veins have  $X_{\text{Mg}} = 0.98 - 0.99$  (Table 4). This is close to the  
324 expected equilibrium value for the partitioning of Fe/Mg between olivine and

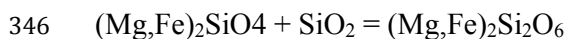
325 orthopyroxene with the secondary olivine composition of  $X_{Mg} = 0.97$  (Koch-Muller et  
326 al. 1992; von Seckendorff and O'Neill 1993).

327

### 328 **Balanced reaction for formation of orthopyroxene veins**

329 The textures indicate that olivine is replaced by orthopyroxene and pore space, and  
330 the chemical data shows that both olivine and orthopyroxene have homogenous  
331 compositions (although there are some small variations). It is possible that some of  
332 the pore space along sub-grain boundaries in olivine could represent initial added  
333 fluid and formed prior to reaction. However, the presence of pores along interphase  
334 boundaries between olivine and orthopyroxene (Figure 3D), along interphase  
335 boundaries between secondary orthopyroxene and clinopyroxene (Figure 3B) and  
336 within secondary orthopyroxene (Figure 3D) demonstrates that porosity forms during  
337 reaction. The relative proportions of orthopyroxene and pore space were determined  
338 from area percentages of BSE images using ImageJ software. Three different regions  
339 in the orthopyroxene veins within sample OP016 (Fig 3D) gave an orthopyroxene to  
340 pore space ratio of 87:13. The results were consistent over areas with minimal (30%  
341 of total area) and extensive (55% of total area) vein formation. Therefore, in a volume  
342 balanced reaction (an area with thickness of 1  $\mu\text{m}$ ), 1  $\mu\text{m}^3$  volume unit of olivine  
343 appears to form approximately 0.87  $\mu\text{m}^3$  of orthopyroxene + 0.13  $\mu\text{m}^3$  of pore space.  
344 The reaction can be described by the equation;

345



347

348 Using the molar volumes of olivine ( $43.67 \text{ cm}^3/\text{mol}$ ) and orthopyroxene ( $62.76$   
349  $\text{cm}^3/\text{mol}$  – calculated using Brey et al 1999), the following, volume balanced reaction,  
350 describes the proportions of orthopyroxene and pore space observed;

351

352  $0.7 \text{ olivine} + 0.3 \text{ pore space} = 0.87 \text{ orthopyroxene} + 0.13 \text{ pore space}$

353

354 As the reaction has a positive  $\Delta V$ , porosity should be consumed during the formation  
355 of orthopyroxene. The presence of porosity could mean that there are two stages to  
356 the reaction whereby olivine first dissolves, forming porosity, and then orthopyroxene  
357 is precipitated and porosity is consumed. The presence of pores along sub-grain  
358 boundaries in the samples could indicate the presence of an initial dissolution  
359 dominated first stage to the reaction. An alternative explanation is that not all of the  
360 dissolved olivine forms orthopyroxene and that a loss of mass during reaction results  
361 in pore space. It has been shown that in many other reactions porosity forms in both  
362 positive and negative  $\Delta V$  (Putnis 2002; Putnis 2009). Porosity is not only related to  
363 volume changes but also the solubility of phases in the fluid (Putnis 2002).

364

365

366 **Formation conditions of metasomatic orthopyroxene in the mantle wedge by**  
367 **slab-derived fluids**

368 Reactions between slab derived Si-rich fluids and olivine dominated mantle  
369 lithologies in the mantle wedge will inevitably lead to the consumption of olivine and  
370 the formation of orthopyroxene. This has been demonstrated in experimental studies  
371 (Keller et al., 2008; Perchuk and Yapaskurt, 2013), and in natural samples of sub-arc  
372 xenoliths (Smith and Riter, 1997; Smith et al., 1999; McInnes et al. 2001; Franz et al.,

373 2002; Arai et al., 2003; Downes et al., 2004; Berly et al., 2006; Morishita et al., 2006;  
374 Ishimaru and Arai, 2011; Vrijmoed et al., 2013). Pressure and temperature data from  
375 these studies are given in Table 6. Pressures range from 0.8–3.4 GPa indicating that  
376 these reactions can occur from top slab conditions to mid to lower crustal conditions  
377 following the geotherm in the mantle wedge. Most temperature estimates for the  
378 reactions in natural samples are approximately 800–900 °C (table 6), suggesting that  
379 metasomatic orthopyroxene forms within a relatively narrow temperature range.

380 Our experiments, although at the lower end of this pressure range, are  
381 consistent with these estimates. The experiments in this study also show that the  
382 orthopyroxene veins will form in fluids consisting of both NaCl poor fluids (no added  
383 NaCl) and NaCl-rich brines (2 M and 8 M) as long as a high fluid : rock ratio is  
384 maintained (>1 wt% fluid). Reactions are also concentrated at grain boundaries and  
385 fractures in the primary olivine. This is also observed in many natural examples  
386 (Grégoire et al., 2001; McInnes et al., 2001). Increasing the fluid amount, salinity  
387 (Fig. 8), fractures, and total grain surface area will increase the amounts of the  
388 reaction.

389

### 390 **Fluid evolution from slab to crust**

#### 391 *Al, Ca, and Cr*

392 Metasomatic orthopyroxene is often characterized by having lower Al, Ca, and Cr  
393 than primary orthopyroxenes (for examples see Smith and Riter, 1997; Smith et al.,  
394 1999; McInnes et al. 2001; Downes et al., 2004; Morishita et al., 2003). Figure 7  
395 shows that this is generally the case but there is a significant amount of scatter in the  
396 data with secondary and primary orthopyroxenes often having similar Al, Ca, and Cr  
397 contents (Table 4). Secondary orthopyroxene in our experiments is generally much

398 higher in Al than secondary orthopyroxene from natural samples. Experimental  
399 orthopyroxenes have Ca contents that are comparable to most of the natural  
400 orthopyroxene data except for some extremely Ca depleted natural samples. Higher  
401 Al in secondary orthopyroxene has also been observed for other experiments in the  
402 same system at higher pressures of 1.8 GPa (Keller et al., 2008). From these  
403 experiments there are no clear trends or variations in Al, Ca, and Cr in orthopyroxene  
404 or clinopyroxene with pressure and temperature. As Al appears to decrease and Ca  
405 appears to increase in the presence of NaCl brines, variations in Al and Ca in  
406 secondary orthopyroxenes are unlikely to be explained by variations in the NaCl  
407 content in the metasomatizing fluids (Tables 1, 4, and 5).

408         One potential explanation for the variance in Al and Ca (and also perhaps Cr)  
409 in secondary orthopyroxene is that concentrations of these elements may vary in the  
410 metasomatizing fluids from one location to another or that the fluid compositions are  
411 modified during reaction with the peridotite. Consider a fracture zone acting as a  
412 conduit for fluid flow. The fluid composition is not dramatically altered as it passes  
413 within the fracture zone (Zack and John, 2007). However, fluid percolation through  
414 the surrounding wall rock perpendicular to the fracture zone may react with olivine in  
415 the peridotite to form orthopyroxene. Precipitation of a zone of Al and Ca rich phases  
416 in the form of garnet and clinopyroxene, close to the fluid source, with a more  
417 orthopyroxene rich zone at the peridotite contact, has been observed by both  
418 Vrijmoed et al. (2013) and Keller et al. (2008). In these experiments, amphibole and  
419 clinopyroxene that form at the contact with the plagioclase matrix represent the more  
420 Al and Ca rich reaction zone. With greater length scales (meters) in natural  
421 metasomatized peridotite (Vrijmoed et al., 2013), the orthopyroxene contains much  
422 less Al<sub>2</sub>O<sub>3</sub> (0.53-0.9) and CaO (0.21-0.24) compared to Al<sub>2</sub>O<sub>3</sub> (3.03-4.68) and CaO

423 (0.61-0.73) in orthopyroxene from the experiments of Keller et al. (2008) and this  
424 study ( $\text{Al}_2\text{O}_3 = 3.39$  and  $\text{CaO} = 0.51$ ), which have much smaller length scales  
425 (microns). This would appear to explain why the Al and Ca contents of secondary  
426 orthopyroxenes vary so much.

427

#### 428 *Mg and Fe*

429 The very high xMg contents of the product phases raise concerns that some Fe might  
430 have been lost to the Pt capsules during the experimental runs, whilst we cannot rule  
431 this out our results are consistent with the relationship between pressure and xMg for  
432 natural samples (Fig. 9). Very high xMg values have been observed in several studies  
433 of natural samples (Morishita et al. 2003; Ishimaru and Arai 2011) also imply that our  
434 results are not extraordinary. Additionally, it seems unlikely that during dissolution of  
435 olivine Fe can instantaneously be diffused to the capsule walls several hundred  
436 microns away but not incorporated into the product phases across the reaction  
437 interface that can be less than a micron, unless the partitioning of Fe/Mg between the  
438 product phases and fluid is low.

439 Using the data in Table 6, XMg appears to decrease with increasing pressure  
440 in both orthopyroxene and clinopyroxene (Figure 9a). This trend fits both the natural  
441 and experimental data, but is unlikely to represent phase stability over pressure as  
442 ferrosilite has a greater molar volume relative to enstatite. It could be related to the  
443 composition of the metasomatic fluid changing with pressure, i.e. indicating a  
444 possible signature of fluid evolution as it passes from the slab through the mantle  
445 wedge. Experimental peridotite – fluid partitioning experiments by Ayers et al. (1997)  
446 showed that the rock / fluid partition coefficients appear to change with pressure. At  
447 2.0 GPa and 900 °C  $D_{\text{Mg}}^{\text{rock/fluid}} = 82.5$  and  $D_{\text{Fe}}^{\text{rock/fluid}} = 32.1$ . At 3.0 GPa and 900 °C,

448  $D_{\text{Mg}}^{\text{rock/fluid}} = 10.1$  and  $D_{\text{Fe}}^{\text{rock/fluid}} = 9.3$ . Although this represents a very limited data  
449 set, this does suggest that at higher pressures pyroxene bearing vein assemblages will  
450 be more Fe rich than at lower pressures. This might explain the trends shown in  
451 Figure 9. Therefore, slab derived fluids should produce increasingly Mg rich  
452 pyroxenite veins as they move to shallower pressures.  $D^{\text{rock/fluid}}$  for Mg also increases  
453 relative to Fe as temperature increases (Ayers et al., 1997), although it appears to have  
454 a lesser effect compared to pressure.

455

## 456 **IMPLICATIONS**

457 Whilst both slab derived fluids and melts are important metasomatic agents in the  
458 mantle wedge, this work specifically focuses on the role of fluid driven reactions. The  
459 experiments presented here clearly demonstrate that the reaction between slab-derived  
460 fluids and olivine will form orthopyroxene veins similar to those observed in  
461 xenoliths from the mantle wedge. Sharp compositional changes across the interfaces  
462 between olivine and orthopyroxene indicate that this reaction is rate limited by  
463 interfacial processes (dissolution and precipitation). At high fluid : rock ratios, an  
464 interconnected grain boundary facilitates fast diffusion rates of elements during  
465 reaction (Rubie 1986; Gardés et al. 2012).

466 A review of the literature on orthopyroxene formed by fluids within the  
467 mantle wedge shows that this reaction occurs over a narrow temperature range ~800-  
468 900°C but a wide pressure range >0.8-3.4 GPa. This means that secondary  
469 orthopyroxenite veins may develop by reaction with slab derived fluids at these  
470 temperatures from the slab interface to the lower arc crust above a subduction zone.  
471 The composition of secondary metasomatic phase is controlled by variation in fluid  
472 compositions, which may vary over cm-m scales (Al + Ca + Cr) during reaction or

473 (Mg / Fe) due to differences in the partitioning behavior at different pressures (km  
474 scale).

475         The results from these experiments enhance our understanding of the chemical  
476 fluxes from slab to crust. Whilst channelized flow of slab fluids may pass rapidly  
477 through the mantle with little modification, the mantle wall rock will become  
478 significantly metasomatized and these reactions may control the composition of the  
479 mantle source regions that arc-magmas are derived from.

480

#### 481 **ACKNOWLEDGEMENTS**

482 The authors would like to thank Kristof Kusebauch for supplying the plagioclase  
483 starting material and Ralf Milke for helpful discussions. The GFZ is thanked for the  
484 use of the piston cylinder and EPMA facilities. Ananya Mallik and an anonymous  
485 reviewer are thanked for their constructive reviews and comments on the paper, as  
486 well as Susanne Straub for further comments and editorial handling of the manuscript.

487 **BIBLIOGRAPHY**

- 488 Arai, S., Ishimaru, S., and Okrugin, V.M. (2003). Metasomatized harzburgite  
489 xenoliths from Avacha volcano as fragments of mantle wedge of the Kamchatka arc:  
490 implication for the metasomatic agent. *The Island Arc*, 12, 233-246.
- 491 Arai, S., Takada, S., Michibayashi, K., and Kida, M. (2004). Petrology of peridotite  
492 xenoliths from Iraya Volcano, Philippines, and its implication for dynamic mantle-  
493 wedge processes. *Journal of Petrology*, 45, 369-389.
- 494 Ayers, J. C., Dittmer, S. K., and Layne, G. D. (1997). Partitioning of elements  
495 between peridotite and H<sub>2</sub>O at 2.0–3.0 GPa and 900–1100° C, and application to  
496 models of subduction zone processes. *Earth and Planetary Science Letters*, 150, 381-  
497 398.
- 498 Bakker, R.J., and Jansen, J.B.H., (1994). A mechanism for preferential H<sub>2</sub>O leakage  
499 from fluid inclusions in quartz, based on TEM observations. *Contributions to*  
500 *Mineralogy and Petrology*, 116, 7-20.
- 501 Bell, D.R., Grégire, M., Grove, T.L., Chatterjee, N., Carlson, R.W., and Buseck, P.R.  
502 (2005). Silica and volatile-element metasomatism of Archean mantle: a xenolith-scale  
503 example from the Kaapvaal Craton. *Contributions to Mineralogy and Petrology*, 150,  
504 251-267.
- 505 Bénard, A., and Ionov, D.A. (2013). Melt- and fluid-rock interaction in supra-  
506 subduction lithospheric mantle: evidence from andesite-hosted veined peridotitic  
507 xenoliths. *Journal of Petrology*, 54, 2339-2378.
- 508 Berly, T. J., Hermann, J., Arculus, R. J., and Lapierre, H. (2006). Supra-subduction  
509 zone pyroxenites from San Jorge and Santa Isabel (Solomon Islands). *Journal of*  
510 *Petrology*, 47, 1531-1555.
- 511 Bishop, F.C., Smith, J.V., and Dawson, J.B. (1978). Na, K, P and Ti in garnet,  
512 pyroxene and olivine from peridotite and eclogite xenoliths from African kimberlites.  
513 *Lithos*, 2, 155-173.
- 514 Botcharnikov, R.E., Kopke, J., Holtz, F., and Wilke, M. (2005). The effect of water  
515 activity on the oxidation and structural state of Fe in a ferro-basaltic melt. *Geochimica*  
516 *et Cosmochimica Acta*, 69, 5071-5085.
- 517 Brey, G.P., Doroshev, A.M., Girmis, A.V., and Turkin, A.I. (1999). Garnet-spinel-  
518 olivine-orthopyroxene equilibria in the FeO-MgO-Al<sub>2</sub>O<sub>3</sub>-SiO<sub>2</sub>-Cr<sub>2</sub>O<sub>3</sub> system: I.  
519 composition and molar volumes of minerals. *European Journal of Mineralogy*, 11,  
520 599-617.

- 521 Downes, H., Macdonald, R., Upton, B.G.J., Cox, K.G., Bodinier, J-L., Mason, P.R.D.,  
522 James, D., Hill, P.G., and Hearn, B.C. Jr. (2004). Ultramafic xenoliths from the  
523 Bearpaw Mountains, Montana, USA: evidence for multiple metasomatic events in the  
524 lithospheric mantle beneath the Wyoming craton. *Journal of Petrology*, 45, 1631-  
525 1662.
- 526 Franz, L., Becker, K-P., Kramer, W., and Herzig, P.M. (2002). Metasomatic mantle  
527 xenoliths from the Bismark Microplate (Papua New Guinea)- thermal evolution,  
528 geochemistry and extent of slab-induced metasomatism. *Journal of Petrology*, 43,  
529 315-343.
- 530 Frezzotti, M. L., Ferrando, S., Peccerillo, A., Petrelli, M., Tecce, F., and Perucchi, A.  
531 (2010). Chlorine-rich metasomatic H<sub>2</sub>O-CO<sub>2</sub> fluids in amphibole-bearing peridotites  
532 from Injibara (Lake Tana region, Ethiopian plateau): Nature and evolution of volatiles  
533 in the mantle of a region of continental flood basalts. *Geochimica et Cosmochimica*  
534 *Acta*, 74, 3023-3039.
- 535 Gardés, E., Wunder, B., Marquardt, K., and Heinrich, W. (2012) The effect of water  
536 on intergranular mass transport: new insights from diffusion-controlled reaction rims  
537 in the MgO-SiO<sub>2</sub> system. *Contributions to Mineralogy and Petrology*, 164, 1-16.
- 538 Grant, T.B., Milke, R., Wunder, B., Wirth, R., and Rhede, D. (2014) Experimental  
539 study of phlogopite reaction rim formation on olivine in phonolite melts; kinetics,  
540 reaction rates and residence times. *American Mineralogist*,
- 541 Grégoire, M., McInnes, B.I.A., and O'Reilly, S.Y. (2001). Hydrous metasomatism of  
542 oceanic sub-arc mantle, Lihir, Papua New Guinea Part 2. Trace element  
543 characteristics of slab-derived fluids. *Lithos*, 59, 91-108.
- 544 Grégoire, M., Jago, S., Maury, R.C., Polve, M., Payot, B., Tamayo, R.A. Jr., and  
545 Yumul, G.P.Jr. (2008). Metasomatic interactions between slab-derived melts and  
546 depleted mantle: insights from xenoliths within Monglo adakite (Luzon arc,  
547 Philippines). *Lithos*, 103, 415-430.
- 548 Hansteen, T.H., Andersen, T., Neumann, E.R., and Jelsma, H. (1991). Fluid and  
549 silicate glass inclusions in ultramafic and mafic xenoliths from Hierro, Canary  
550 Islands: implications for mantle metasomatism. *Contributions to Mineralogy and*  
551 *Petrology*, 107, 242-254.
- 552 Herman, J., Spandler, C., Hack, A., and Korsakov, A.V. (2006). Aqueous fluids and  
553 hydrous melts in high-pressure and ultra-high pressure rocks: implications for element  
554 transfer in subduction zones. *Lithos*, 92, 399-417.

- 555 Ishimaru, S., Arai, S., Ishida, Y., Shirasaka, M., and Okrugin, V.M. (2007). Melting  
556 and multi-stage metasomatism in the mantle wedge beneath a frontal arc inferred  
557 from highly depleted peridotite xenoliths from the Avacha Volcano, Southern  
558 Kamchatka. *Journal of Petrology*, 48, 395-433.
- 559 Ishimaru, S., and Arai, S. (2009). Highly silicic glasses in peridotite xenoliths from  
560 Avacha volcano, Kamchatka arc; implications for melting and metasomatism within  
561 the sub-arc mantle. *Lithos*, 107, 93-106.
- 562 Ishimaru, S., and Arai, S. (2011). Peculiar Mg-Ca-Si metasomatism along a shear  
563 zone within the mantle wedge: inference from fine-grained xenoliths from Avacha  
564 volcano, Kamchatka. *Contributions to Mineralogy and Petrology*, 161, 703-720.
- 565 Johannes W. (1973) Eine vereinfachte Piston-Zylinder-Apparatur hoher Genauigkeit.  
566 *Neues Jahrbuch Mineralogi* 337-351
- 567 Johannes W., Bell P.M., Mao H.K., Boettcher A.L., Chipman D.W., Hays J.F.,  
568 Newton R.C., and Seifert F. (1971) An interlaboratory comparison of piston-cylinder  
569 pressure calibration using the albite-breakdown reaction. *Contributions to Mineralogy  
570 and Petrology*, 32, 24-38
- 571 Keller, L.M., Wunder, B., Rhede, D., and Wirth, R. (2012). Component mobility at  
572 900°C and 18 kbar from experimentally grown coronas in natural gabbro. *Geochimica  
573 et Cosmochimica Acta*, 72, 4307-4322.
- 574 Koch-Müller M., Cemic L., and Langer K. (1992). Experimental and thermodynamic  
575 study of Fe-Mg exchange between olivine and orthopyroxene in the system MgO-  
576 FeO-SiO<sub>2</sub>. *European Journal of Mineralogy*, 4, 115-135
- 577 Konzett, J., Rhede, D., and Frost, D.J. (2012). The high PT stability of apatite and Cl  
578 partitioning between apatite and hydrous potassic phases in peridotite: an  
579 experimental study to 19 GPa with implications for the transport of P, Cl and K in the  
580 upper mantle. *Contributions to Mineralogy and Petrology*, 163, 277-296.
- 581 Lespinasse, M., and Cathelineau, M. (1990). Fluid percolations in a fault zone: a  
582 study of fluid inclusion planes in the St Sylvestre granite, northwest Massif Central,  
583 France. *Tectonophysics*, 184, 173-187.
- 584 Liu, Y., Olsen, A.A., and Rimstidt, J.D. (2006) Mechanism for the dissolution of  
585 olivine series minerals in acidic solutions. *American Mineralogist*, 91, 455-458.
- 586 Malaspina, N., Herman, J., Scambelluri, M., and Compagnoni, R. (2006). Polyphase  
587 inclusions in garnet-orthopyroxenite (Dabie Shan, China) as monitors for

- 588 metasomatism and fluid-related trace element transfer in subduction zone peridotite.  
589 Earth and Planetary Science Letters, 249, 173-187.
- 590 Malik, A., Nelson, J., and Dasgupta, R. (2015). Partial melting of fertile peridotite  
591 fluxed by hydrous rhyolitic melt at 2-3 GPa: implications for mantle wedge  
592 hybridization by sediment melt and generation of ultrapotassic magmas at convergent  
593 margins. Contributions to Mineralogy and Petrology, 169, 48.
- 594 Mallmann, G., and O'Neill, H.St.C. (2009). The crystal/melt partitioning of V during  
595 mantle melting as a function of oxygen fugacity compared with some other elements  
596 (Al, P, Ca, Sc, Ti, Cr, Fe, Ga, Y, Zr, Nb). Journal of Petrology, 50, 1765-1794.
- 597 Mallmann, G., O'Neill, H.St.C., and Klemme, S. (2009). Heterogeneous distribution  
598 of phosphorus in olivine from otherwise well-equilibrated spinel peridotite xenoliths  
599 and its implication for the mantle geochemistry of lithium. Contributions to  
600 Mineralogy and Petrology, 158, 485-504.
- 601 Manning, C.E. (2004). The chemistry of subduction zone fluids. Earth and Planetary  
602 Science Letters, 223, 1-16.
- 603 Marschall, H.R., and Schumacher, J.C. (2012). Arc magmas sources from melange  
604 diapirs in subduction zones. Nature Geoscience, 862-867.
- 605 Massare, D., Metrich, N., and Clocchiatti, R. (2002). High-temperature experiments  
606 on silicate melt inclusions in olivine at 1 atm: inference on temperatures of  
607 homogenization and H<sub>2</sub>O concentrations. Chemical Geology, 183, 87-98.
- 608 McInnes, B.I.A., Gregoire, M., Binns, R.A., Herzig, P.M., and Hannington, M.D.  
609 (2001) Hydrous metasomatism of oceanic sub-arc mantle, Lihir, Papua New Guinea:  
610 petrology and geochemistry of fluid-metasomatised mantle wedge xenoliths. Earth  
611 and Planetary Science Letters, 188, 169-183.
- 612 Médard, E., McCammon, C.A., Barr, J.A., and Grove, T.L. (2008). Oxygen fugacity,  
613 temperature reproducibility, and H<sub>2</sub>O contents of nominally anhydrous piston-  
614 cylinder experiments using graphite capsules. *American Mineralogist*, 93, 1838-1844.
- 615 Millman-Barris, M.S., Beckett, J.R., Baker, M.B., Hofmann, A.E., Morgan, Z.,  
616 Crowley, M.R., Vielzeuf, D., and Stolper, E. (2008). Zoning of phosphorus in igneous  
617 olivine. Contributions to Mineralogy and Petrology, 155, 739-765.
- 618 Milke, R., Kolzer, K., Koch-Müller, M., and Wunder, B. (2009) Orthopyroxene rim  
619 growth between olivine and quartz at low temperatures (750-950°C) and low water  
620 concentration. Mineralogy and Petrology, 97, 223-232.

- 621 Milke, R., Abart, R., Keller, L., and Rhede, D. (2011) The behavior of Mg, Fe, and Ni  
622 during the replacement of olivine by orthopyroxene: experiments relevant to mantle  
623 metasomatism. *Mineralogy and Petrology*, 103, 1-8.
- 624 Milke, R., Neusser, G., Kolzer, K., and Wunder, B. (2013) Very little water is  
625 necessary to make a dry solid silicate system wet. *Geology*, 41, 247-250.
- 626 Morishita, T., Arai, S., and Green, D.H. (2003). Evolution of low-Al orthopyroxene in  
627 the Horoman Peridotite, Japan: an unusual indicator of metasomatizing fluids. *Journal*  
628 *of Petrology*, 44, 1237-1246.
- 629 Perchuk, A.L., and Yapaskurt, V.O. (2013). Experimental simulation of  
630 orthopyroxene enrichment and carbonation in the suprasubduction mantle under the  
631 influence of H<sub>2</sub>O, CO<sub>2</sub> and SiO<sub>2</sub>. *Geochemistry International*, 51, 257-268.
- 632 Pokrovsky, O.S. and Schott, J. (2000) Kinetics and mechanism of forsterite  
633 dissolution at 25°C and pH from 1 to 12. *Geochimica et Cosmochimica Acta*, 64,  
634 3313-3325.
- 635 Portnyagin, M., Almeev, R., Matveev, S., and Holtz, F. (2008). Experimental  
636 evidence for rapid water exchange between melt inclusions in olivine and host  
637 magma. *Earth and Planetary Science Letters*, 272, 541-552.
- 638 Prouteau, G., Scaillet, B., Pichavant, M., and Maury, R. (2001) Evidence for mantle  
639 metasomatism by hydrous silicic melts derived from subducted oceanic crust. *Nature*,  
640 410, 197-200.
- 641 Putnis, A. (2002). Mineral replacement reactions: from macroscopic observations to  
642 microscopic mechanisms. *Mineralogical Magazine*, 66, 689-708.
- 643 Putnis, A. (2009). Mineral replacement reactions. *Reviews in Mineralogy and*  
644 *Geochemistry*, 70, 87-124.
- 645 Rapp, R.P., Shimizu, N., Norman, M.D., and Applegate, G.S. (1999). Reaction  
646 between slab-derived melts and peridotite in the mantle wedge: experimental  
647 constraints at 3.8 GPa. *Chemical Geology*, 160, 335-356.
- 648 Rapp, R.P., Norman, M.D., Laporte, D., Yaxley, G.M., Martin, H., and Foley, S.F.  
649 (2010). Continent formation in the Archean and chemical evolution of the cratonic  
650 lithosphere: melt-rock reaction experiments at 3-4 GPa and petrogenesis of Archean  
651 Mg-diorites (sanukitoids). *Journal of Petrology*, 51, 1237-1266.
- 652 Rubie, D.C. (1986). The Catalysis of mineral reactions by water and restrictions on  
653 the presence of aqueous fluid during metamorphism. *Mineralogical Magazine*,  
654 50, 399-415.

- 655 Schiano, P., Clocchiatti, R., Shimizu, Maury, R.C., Jochum, K.P., and Hofmann,  
656 A.W. (1995). Hydrous, silica-rich melts in the sub-arc mantle and their relationships  
657 with erupted arc lavas. *Nature*, 377, 595-600.
- 658 Smith, D., and Riter, J.C.A. (1997). Genesis and evolution of low-Al orthopyroxene  
659 in spinel peridotite xenoliths, Grand Canyon field, Arizona, USA. *Contributions to*  
660 *Mineralogy and Petrology*, 127, 391-404.
- 661 Smith, D., Riter, J.C.A., and Mertzman, S.A. (1999). Water-rock interactions,  
662 orthopyroxene growth, and Si-enrichment in the mantle: evidence in xenoliths from  
663 the Colorado Plateau, southwestern United States. *Earth and Planetary Science*  
664 *Letters*, 165, 45-54.
- 665 Spandler, C., and Pirard, C. (2013). Element recycling from subducting slabs to arc  
666 crust: a review. *Lithos*, 170-171, 208-223.
- 667 Sommer, H., Regenauer-Lieb, K., Gasharova, B., and Siret, D. (2008). Grain  
668 boundaries: a possible water reservoir in the Earth's mantle? *Mineralogy and*  
669 *Petrology*, 94, 1-8.
- 670 Soustelle, V., Tommasi, A., Demouchy, S., and Ionov, D.A. (2010). Deformation and  
671 Fluid-Rock Interaction in the Supra-subduction Mantle: Microstructures and Water  
672 Contents in Peridotite Xenoliths from the Avacha Volcano, Kamchatka. *Journal of*  
673 *Petrology*, 51, 363-394.
- 674 Soustelle, V., Tommasi, A., Demouchy, S., and Franz, L. (2011). Melt-rock  
675 interactions, deformation, hydration and seismic properties in the sub-arc lithospheric  
676 mantle inferred from xenoliths from seamounts near Lihir, Papua New Guinea.  
677 *Tectonophysics*, 608, 330-345.
- 678 von Seckendorff V., and O'Neill H.S.C. (1993). An experimental study of Fe-Mg  
679 partitioning between olivine and orthopyroxene at 1173, 1273 and 1423 K and 1.6  
680 GPa. *Contributions to Mineralogy and Petrology*, 113, 196-207
- 681 Vrijmoed, J.C., Austrheim, H., John, T., Hin, R.C., Corfu, F., and Davies, G.R.  
682 (2013). Metasomatism in the ultrahigh-pressure Svartberget garnet-peridotite  
683 (Western Gneiss Region, Norway): implications for the transport of crust derived-  
684 fluids within the mantle. *Journal of Petrology*, 54, 1815-1848.
- 685 Yund, R. (1997) Rates of grain boundary diffusion through enstatite and forsterite  
686 reaction rims. *Contributions to Mineralogy and Petrology*, 126, 224-236.
- 687 Zack, T., and John, T. (2007). An evaluation of reactive fluid flow and trace element  
688 mobility in subducting slabs. *Chemical Geology*, 239, 199-216.

689

690

691

692

693

694

695 **Figures**

696 **Figure 1:** Experimental set-up.

697

698 **Figure 2:** BSE images of cracks and veins in olivine. Figure 2 – Image from sample  
699 OP004 shows different types of cracks or veins. These include unfilled cracks that  
700 cross-cut other features and formed during unloading of pressure; trails of small <1  
701  $\mu\text{m}$  pores; and linear patches of secondary more Mg-rich olivine that are interspaced  
702 with large pores 1-2  $\mu\text{m}$  pores. For further details on these types see text. Figure 2b –  
703 image of sample OP010 shows an area of secondary olivine formation near a crack  
704 and large pores as well as a type 1 unfilled crack (contains some polishing material).  
705 Line A-B indicates the line scan shown in Figure 4. Note the relatively sharp interface  
706 between secondary olivine (dark grey) and the original olivine (lighter grey).

707

708 **Figure 3:** BSE images of orthopyroxene and orthopyroxene veins. Abbreviations are;  
709 plag – plagioclase, amph – amphibole, cpx – clinopyroxene, opx – orthopyroxene.  
710 Figure 3a – image from sample OP002 shows the reaction rim of amphibole +  
711 clinopyroxene that has formed between olivine and the plagioclase matrix. A large  
712 clinopyroxene vein extends across the olivine to the reaction rim. Secondary Mg-rich  
713 olivine (olivine 2) has also formed in a small zone adjacent to the clinopyroxene vein.  
714 Figure 3b shows a pyroxenite vein extending across the olivine grain from sample

715 OP010. Two clinopyroxene compositions are observed. A complex network of large  
716 pores and cracks are associated within the olivine close to the vein. It is unclear if  
717 these are formed during unloading or due to a fluid. Smaller trails along interphase  
718 boundaries, such as the one highlighted with an arrow between the orthopyroxene  
719 vein and CPX2, are common between each phase within the vein. Figure 3c –  
720 complex vein structure of secondary Mg-rich olivine, clinopyroxene, and pores  
721 observed within sample OP010. Figure 3d shows an interconnected network of  
722 orthopyroxene veins through an olivine grain from sample OP016. The reaction rim  
723 and contact with the matrix is 100 – 200  $\mu\text{m}$  above the top of this image. Some  
724 clinopyroxene is also present in the vein network along with many pores of varying  
725 size ( $< 1 \mu\text{m}$  up to 20  $\mu\text{m}$ ).

726

727 **Figure 4:** Secondary olivine. Line scan across a zone of secondary Mg-rich olivine  
728 from sample OP010. The location of line scan A-B is shown in Figure 2. The location  
729 of the interface between Mg-rich olivine and primary olivine is shown by the grey  
730 dashed lines. Secondary olivine is on the right hand side of the line scan A) and  
731 primary olivine is on the left (B).

732

733

734 **Figure 5:** Line scan across an orthopyroxene vein from sample OP003, where the  
735 left and right sections are olivine and the middle section is the orthopyroxene vein.

736

737 **Figure 6:** Line scan from olivine to orthopyroxene (left to right) from sample OP010.

738

739 **Figure 7:** Plot of Al vs. Ca for the orthopyroxene veins. OPX I (grey circles) is  
740 primary orthopyroxene from sub-arc xenoliths and OPX II is secondary metasomatic  
741 orthopyroxene in sub-arc xenoliths. Analyses are taken from Smith and Riter (1997),  
742 Smith et al. (1999), McInnes et al. (2001), Franz et al. (2002), Arai et al. (2003), Arai  
743 et al. (2004), Downes et al. (2004), Morishita et al. (2004), Berly et al. (2006),  
744 Ishimaru et al. (2007), Grégoire et al. (2008) and Ishirau and Arai (2011). Exp =  
745 analyses of orthopyroxenes from the experiments in this study.

746

747 **Figure 8:** Effects of a NaCl brine on orthopyroxene compositions. Average analyses  
748 of orthopyroxenes from samples OP003 (~0 mol NaCl), OP004 (~2 mol NaCl) and  
749 OP016 (~8 mol NaCl) were used and the error bars correspond to the standard  
750 deviation of the data for each sample.

751

752 **Figure 9:**  $X_{Mg}$  of pyroxenes vs. pressure.  $X_{Mg} = (Mg/(Mg + Fe))$  of metasomatic  
753 orthopyroxene and clinopyroxene from natural (Arai et al. 2003; Berly et al. 2006;  
754 Downes et al. 2004; Franz et al. 2002; McInnes et al. 2001; Morishita et al. 2003;  
755 Smith and Riter 1997; Vrijmoed et al. 2013) and experimental (Keller et al. 2008;  
756 Perchuk and Yapaskurt 2013) samples plotted against the estimated pressure.  
757 Standard deviations in  $X_{Mg}$  are the same as the standard deviations for analyses from  
758 each study, and errors for pressure are the ranges, if given, in the literature.

## Tables

**Table 1.** EPMA analyses (oxide wt%) of starting materials.

	Plagioclase		San Carlos olivine	Apatite
SiO <sub>2</sub>	52.96	(50.01-54.54)	41.86	0.01
Al <sub>2</sub> O <sub>3</sub>	30.7	(29.53-32.71)	-	-
FeO	0.13	(0.00-0.42)	9.25	0.04
MnO	0.02	(0.00-0.12)	0.36	0.05
MgO	0.03	(0.00-0.15)	50.95	-
CaO	12.65	(11.44-14.57)	0.18	54.43
Na <sub>2</sub> O	4.42	(3.40-5.16)	-	-
K <sub>2</sub> O	0.05	(0.03-0.09)	0.04	0.03
P <sub>2</sub> O <sub>5</sub>	0.02	(0.00-0.04)	0.01	42.46
F	-	-	-	-
Cl	0.01	(0.00-0.04)	-	1.09
Total	100.99	-	102.65	98.12
An	0.61	(0.55-0.69)	-	-
Ab	0.39	(0.30-0.44)	-	-
Kfs	-	-	-	-
X <sub>Mg</sub>	-	-	0.9	-

**Table 2.** Experimental conditions.

<b>Experiment</b>	<b>Time(h)</b>	<b>T (°C)</b>	<b>P (MPa)</b>	<b>wt.% fluid</b>	<b>Fluid</b>	<b>Veins</b>
OP001	192	800	800	0	-	-
OP002	192	800	800	0.51	H <sub>2</sub> O	CPX, OI2
OP003	192	800	800	2.04	H <sub>2</sub> O	OPX
OP004	192	800	800	1.99	2M NaCl	OPX, OI2
OP010	192	800	800	1.13	H <sub>2</sub> O	OPX, CPX, OI2
OP012	192	800	800	1.86	H <sub>2</sub> O	-
OP016	192	800	800	1.98	8M NaCl	OPX, CPX

**Table 3.** Representative EPMA analyses (oxide wt%) of olivine.

Experiment	OL2		OI1	
	OP010	OP010	OP010	OP010
SiO <sub>2</sub>	41.981	42.03	40.661	40.7
TiO <sub>2</sub>	0.006	0.011	0.014	-
Cr <sub>2</sub> O <sub>3</sub>	0.034	0.007	0.022	0.017
Al <sub>2</sub> O <sub>3</sub>	0.002	-	0.027	0.023
FeO	2.384	2.738	8.599	8.579
MnO	0.19	0.177	0.172	0.125
NiO	0.317	0.376	0.393	0.442
MgO	55.613	55.229	50.018	50.107
CaO	0.026	0.027	0.1	0.085
Na <sub>2</sub> O	-	0.016	0.015	-
K <sub>2</sub> O	0.008	-	-	0.002
CoO	0.011	0.014	-	0.002
P <sub>2</sub> O <sub>5</sub>	0.024	-	0.01	0.006
Total	100.595	100.625	100.03	100.089
X <sub>Mg</sub>	0.971	0.967	0.905	0.906

OI1 is primary San Carlos olivine, and OI2 is secondary olivine in patches.  
Structural formulae calculated based on four oxygens.  $X_{Mg} = Mg/(Mg+Fe)$ .

**Table 4.** Representative EPMA analyses (oxide wt%) of orthopyroxene.  
 $X_{Mg} = Mg/(Mg+Fe)$ .

Experiment	OP003	OP003	OP004	OP004	OP010	OP010	OP010
SiO <sub>2</sub>	56.36	56.39	57.17	57.24	58.29	57.72	58.03
TiO <sub>2</sub>	0.02	0.02	0.06	0.03	0.04	0.04	0.05
Cr <sub>2</sub> O <sub>3</sub>	0.03	0.03	0.02	0.03	0.01	0.01	0.02
Al <sub>2</sub> O <sub>3</sub>	3.22	2.85	3.13	3.25	2.27	3.19	2.27
FeO	1.57	1.46	1.05	1.12	1	0.77	1.03
MnO	0.14	0.15	0.15	0.17	0.23	0.18	0.22
NiO	0.16	0.17	0.13	0.11	0.15	0.13	0.1
MgO	36.35	36.29	36.33	36.09	37.25	37.38	37.15
CaO	0.53	0.57	0.59	0.6	0.62	0.51	0.83
Na <sub>2</sub> O	0.02	0.02	0.12	0.09	0.05	0.03	0.07
K <sub>2</sub> O	0.01	-	0.01	0.01	-	-	-
CoO	0.02	0.03	0.01	-	-	-	0
P <sub>2</sub> O <sub>5</sub>	0.04	0.05	0.06	0.06	0.06	0.02	0.05
Total	98.47	98.02	98.83	98.8	99.97	99.99	99.82
$X_{Mg}$	0.98	0.98	0.98	0.98	0.99	0.99	0.98

**Table 5.** Representative EPMA analyses (oxide wt%) of clinopyroxene.  
 $X_{Mg} = Mg/(Mg+Fe)$ .

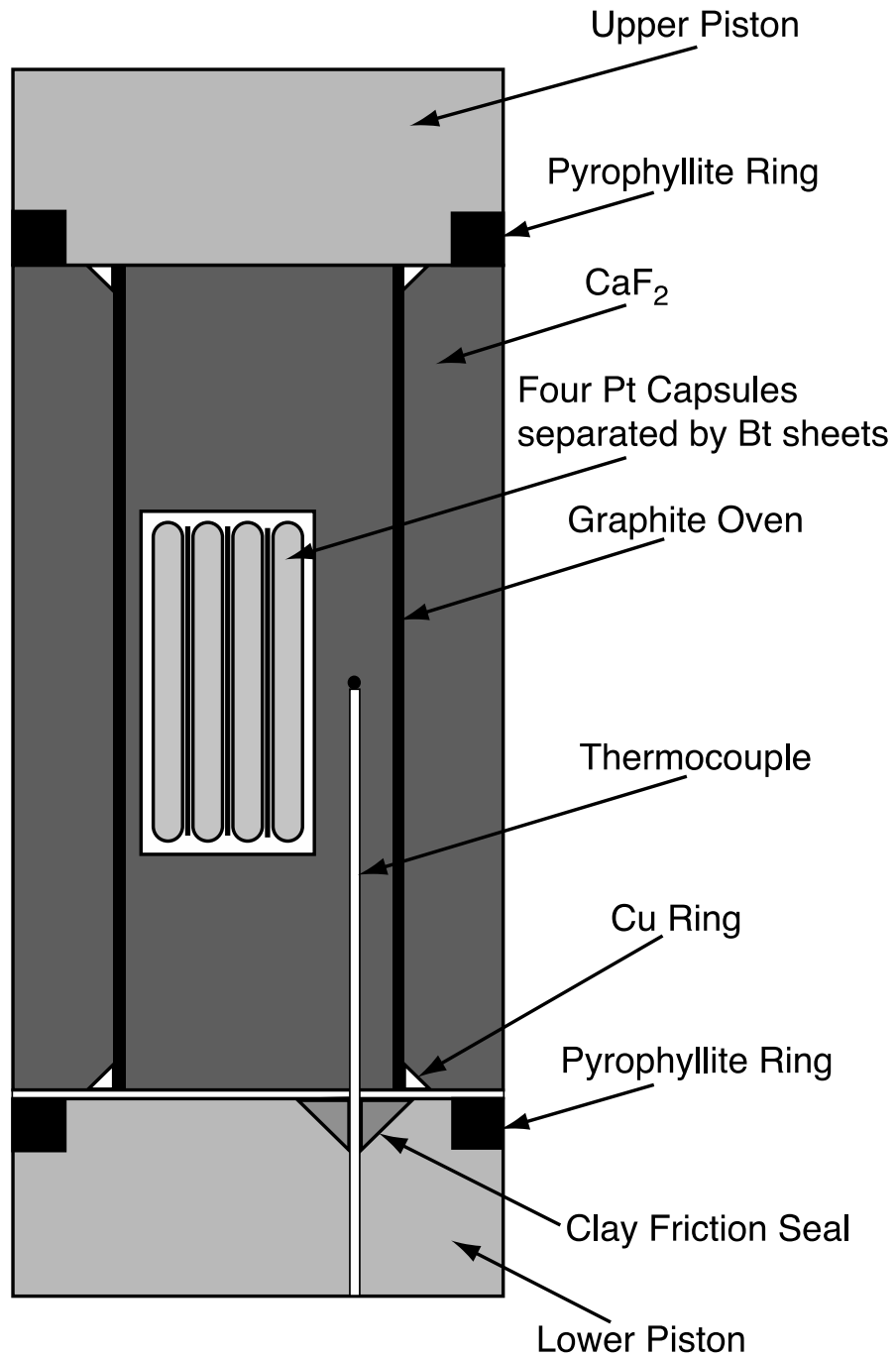
Experiment	OP003	OP010	OP010	OP016	OP016	OP016
SiO <sub>2</sub>	55.09	55.22	56.26	51.67	53.89	53.51
TiO <sub>2</sub>	0.11	0.08	0.25	-	-	-
Cr <sub>2</sub> O <sub>3</sub>	0.05	0.05	0.02	-	-	-
Al <sub>2</sub> O <sub>3</sub>	1.17	0.98	4.65	5.71	2.72	3.37
FeO	0.85	0.75	0.66	1.82	1.58	1.66
MnO	0.11	0.14	0.09	0.36	0.3	0.24
NiO	0.07	0.03	0.12	-	-	-
MgO	18.91	19.69	22.16	15.48	17.5	16.56
CaO	23.98	22.91	10.89	23.62	23.16	23.45
Na <sub>2</sub> O	0.32	0.28	1.06	0.69	0.63	0.74
K <sub>2</sub> O	-	0.03	0.18	-	-	-
CoO	0.02	-	-	-	-	-
P <sub>2</sub> O <sub>5</sub>	0.04	0.2	0.03	0.13	0.15	0.06
Total	100.72	100.36	96.37	99.48	99.94	99.59
$X_{Mg}$	1	0.96	0.98	0.99	0.99	0.98

Table 6.

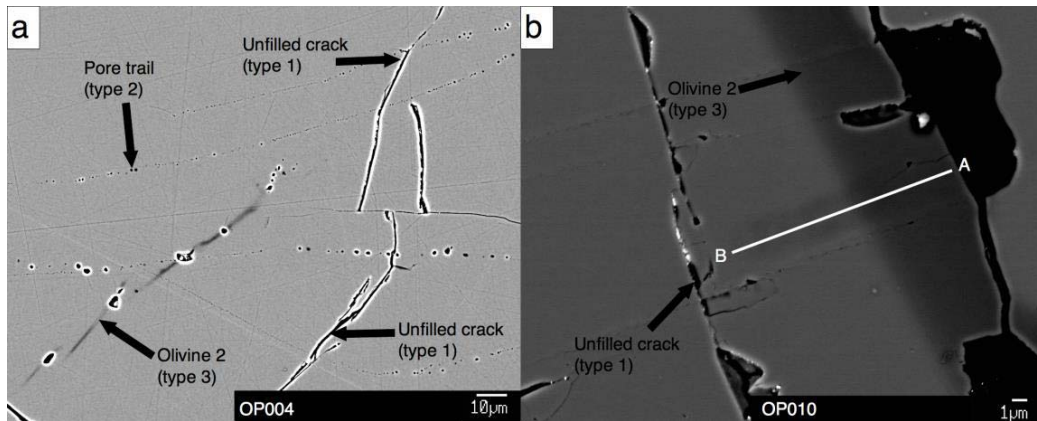
Metasomatic OPX	Pressure (GPa)	Temperature	N	SiO <sub>2</sub>	TiO <sub>2</sub>	Al <sub>2</sub> O <sub>3</sub>	Cr <sub>2</sub> O <sub>3</sub>	MgO	MnO	FeO	CaO	K <sub>2</sub> O	Na <sub>2</sub> O	x Mg
Smith et al. (1999)	-	800	2	58.50 (0)	0.03 (1)	0.58 (54)	0.06 (2)	35.20 (57)	0.16 (4)	5.84 (61)	0.39 (18)	-	0.01 (0)	0.91 (1)
Morishita et al. (2003)	>1.0	900	6	57.80 (91)	0.05 (0)	1.01 (119)	0.09 (7)	35.76 (104)	0.16 (1)	5.30 (38)	0.34 (28)	0.03 (0)	0.03 (1)	0.93 (1)
Franz et al. (2002)	1.3	650-950	9	58.50 (0)	0.03 (1)	0.58 (54)	0.06 (2)	35.20 (57)	0.16 (4)	5.84 (61)	0.39 (18)	-	0.01 (0)	0.91 (1)
Smith and Riter (1997)	1.45	800-850	3	57.93 (67)	0.02 (2)	0.12 (7)	0.06 (5)	35.33 (78)	0.30 (18)	6.59 (118)	0.17 (16)	-	0.01 (1)	0.92 (2)
Berly et al. (2006)	1.3-1.7	870	7	56.70 (61)	0.06 (6)	1.45 (48)	0.50 (9)	33.23 (75)	0.10 (4)	6.98 (70)	0.79 (16)	-	0.20 (9)	0.90 (1)
McInnes et al. (2001)	1.0-2.2	790-1034	3	57.79 (21)	0.01 (0)	1.05 (51)	0.36 (5)	34.25 (175)	0.14 (3)	5.65 (34)	0.30 (11)	-	0.02 (1)	0.92 (1)
Arai et al. (2003)	1.62	900	3	57.11 (53)	0.02 (3)	1.21 (27)	0.03 (4)	35.67 (95)	0.10 (3)	4.61 (59)	0.26 (22)	-	-	0.94 (1)
Arai et al. (2006)	-		7	57.31 (71)	-	1.31 (47)	0.22 (15)	34.50 (65)	0.18 (6)	5.55 (69)	0.47 (22)	-	-	0.92 (1)
Ishimaru and Arai (2011)	-	845-980	10	57.98 (124)	0.01 (1)	0.97 (33)	0.20 (11)	36.67 (140)	0.08 (4)	3.67 (140)	0.55 (11)	-	-	0.96 (2)
Ishimaru et al. (2007)	-	890-1100	11	57.74 (86)	0.01 (2)	1.21 (50)	0.29 (16)	34.99 (78)	0.13 (4)	5.58 (25)	0.66 (32)	-	-	0.92 (1)
Downes et al. (2004)	2.0	830-1090	2	57.48 (24)	-	0.14 (12)	0.05 (5)	33.70 (62)	0.22 (8)	7.21 (5)	0.35 (48)	-	0.04 (1)	0.89 (0)
Vrijmoed et al. (2013)	3.4	800	109	56.6	0.02	0.53	0.03	30.8	0.23	12.2	0.24	-	0.01	0.82
<b>Experimental</b>														
This study	0.8	800	115	56.63 (63)	0.03 (2)	3.38 (71)	0.02 (2)	36.16 (77)	0.23 (9)	1.79 (59)	0.51 (10)	-	0.04 (3)	0.98 (1)
Keller et al. (2008)	1.8	900	8	56.48	0.01	3.03	0.01	32.78	0.08	8.72	0.61	-	0.06	0.88
Keller et al. (2008)	1.8	900	2	53.39	-	4.68	-	31.92	0.12	7.60	0.73	-	-	0.91
Perchuk and Yapaskurt (2013)	2.5	800	1	56.03	0.23	1.55	-	33.50	-	8.04	0.18	0.01	0.17	0.88
<b>Metasomatic CPX</b>														
Morishita et al. (2003)	>1.0	900	3	54.36 (60)	0.12 (3)	0.78 (49)	0.49 (28)	17.65 (31)	0.10 (0)	1.78 (19)	24.26 (17)	0.07 (6)	0.25 (5)	0.97 (2)
Smith and Riter (1997)	1.3	650-950	1	54.40	0.04	0.80	0.09	18.50	0.06	1.85	23.90	-	0.08	0.97
Franz et al. (2002)	1.45	800-850	7	54.71 (102)	0.02 (2)	1.66 (131)	0.21 (21)	19.03 (140)	0.07 (2)	2.91 (115)	21.01 (264)	0.03 (4)	0.16 (8)	0.93 (4)
Berly et al. (2006)	1.3-1.7	870	8	54.10 (80)	0.11 (8)	1.37 (65)	0.68 (21)	17.20 (45)	0.05 (5)	2.81 (83)	24.15 (42)	-	0.26 (9)	0.94 (2)
McInnes et al. (2001)	1.0-2.2	790-1034	3	55.65 (41)	0.02 (1)	1.35 (14)	0.43 (11)	21.49 (82)	0.08 (1)	2.18 (18)	17.78 (158)	0.21 (11)	0.32 (12)	0.95 (0)
Downes et al. (2004)	2.0	830-1090	18	53.69 (66)	0.14 (10)	1.48 (89)	0.53 (40)	16.35 (120)	0.15 (6)	4.31 (190)	22.54 (59)	-	0.57 (24)	0.89 (5)
Vrijmoed et al. (2013)	3.4	800	117	54.90	0.03	1.20	0.42	15.70	0.11	4.53	21.80	0.01	1.07	0.86
<b>Experimental</b>														
This study	0.8	800	14	54.32 (118)	0.06 (4)	2.25 (160)	0.04 (2)	17.92 (135)	0.19 (10)	1.26 (47)	23.26 (55)	0.01 (2)	0.50 (21)	0.98 (1)

Table 6. Composition of secondary orthopyroxene and clinopyroxene from natural and experimental samples.

**Figure 1.**



**Figure 2.**



**Figure 3.**

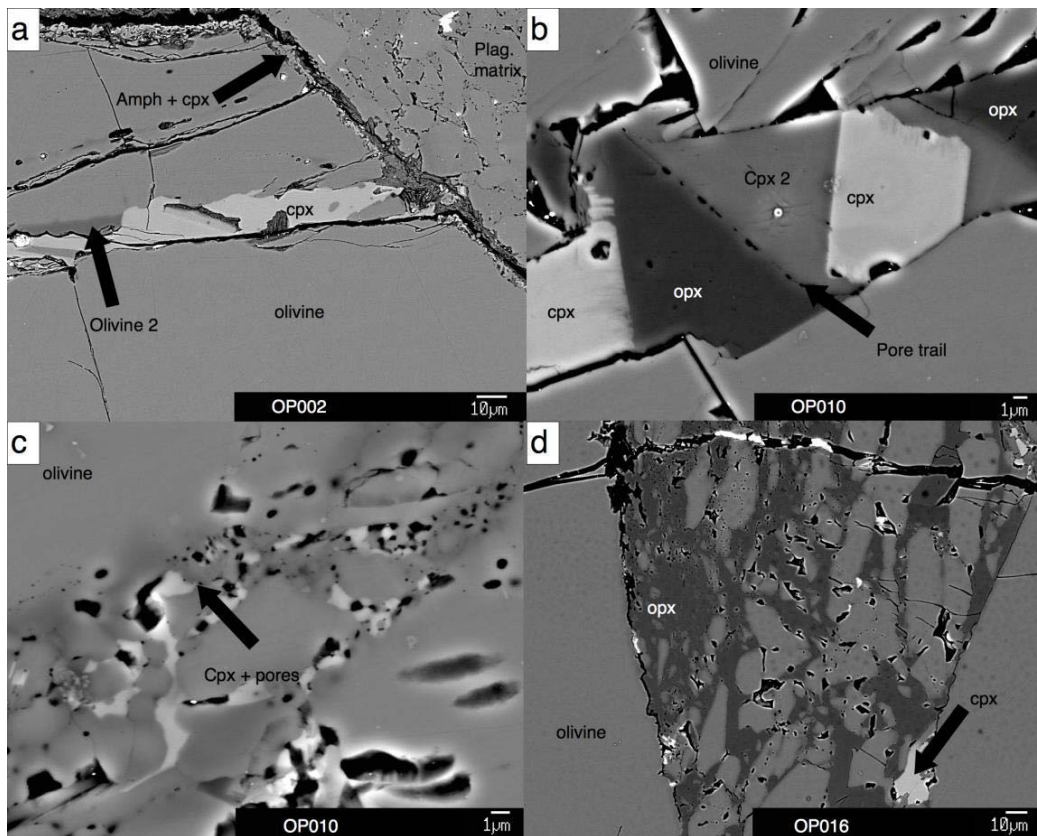


Figure 4.

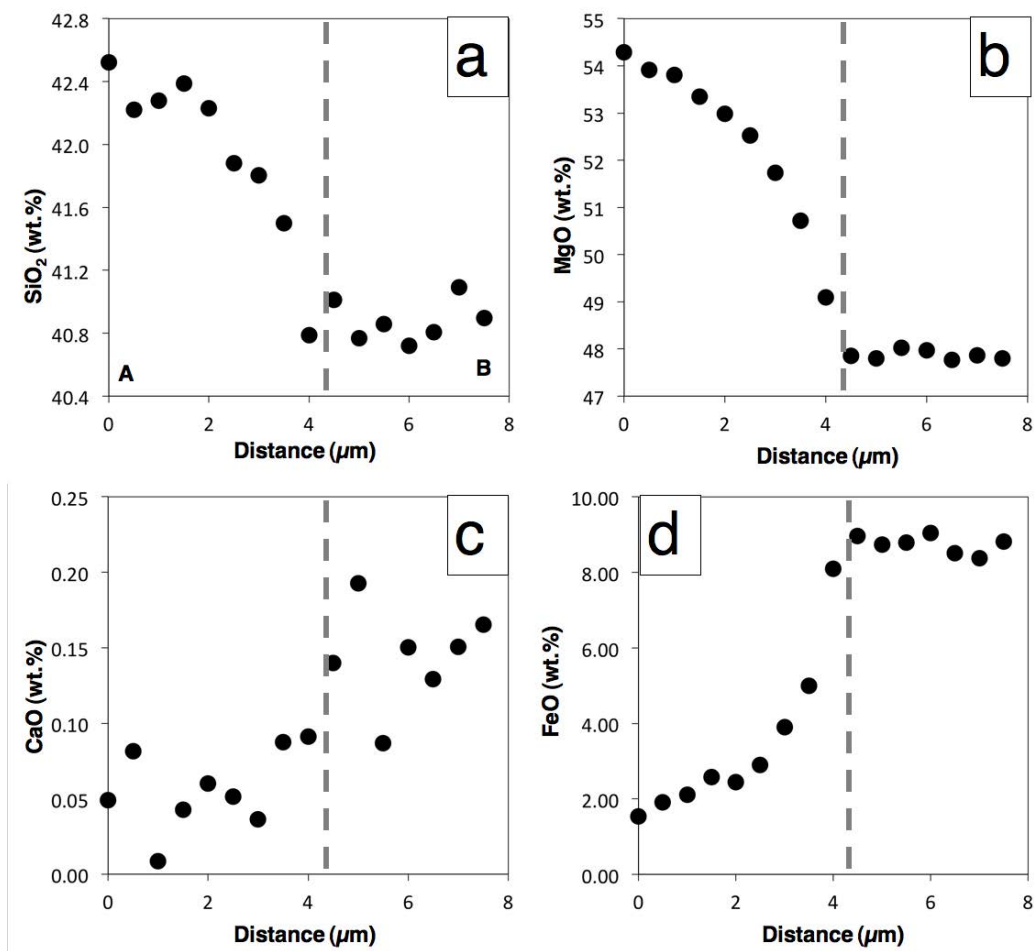


Figure 5.

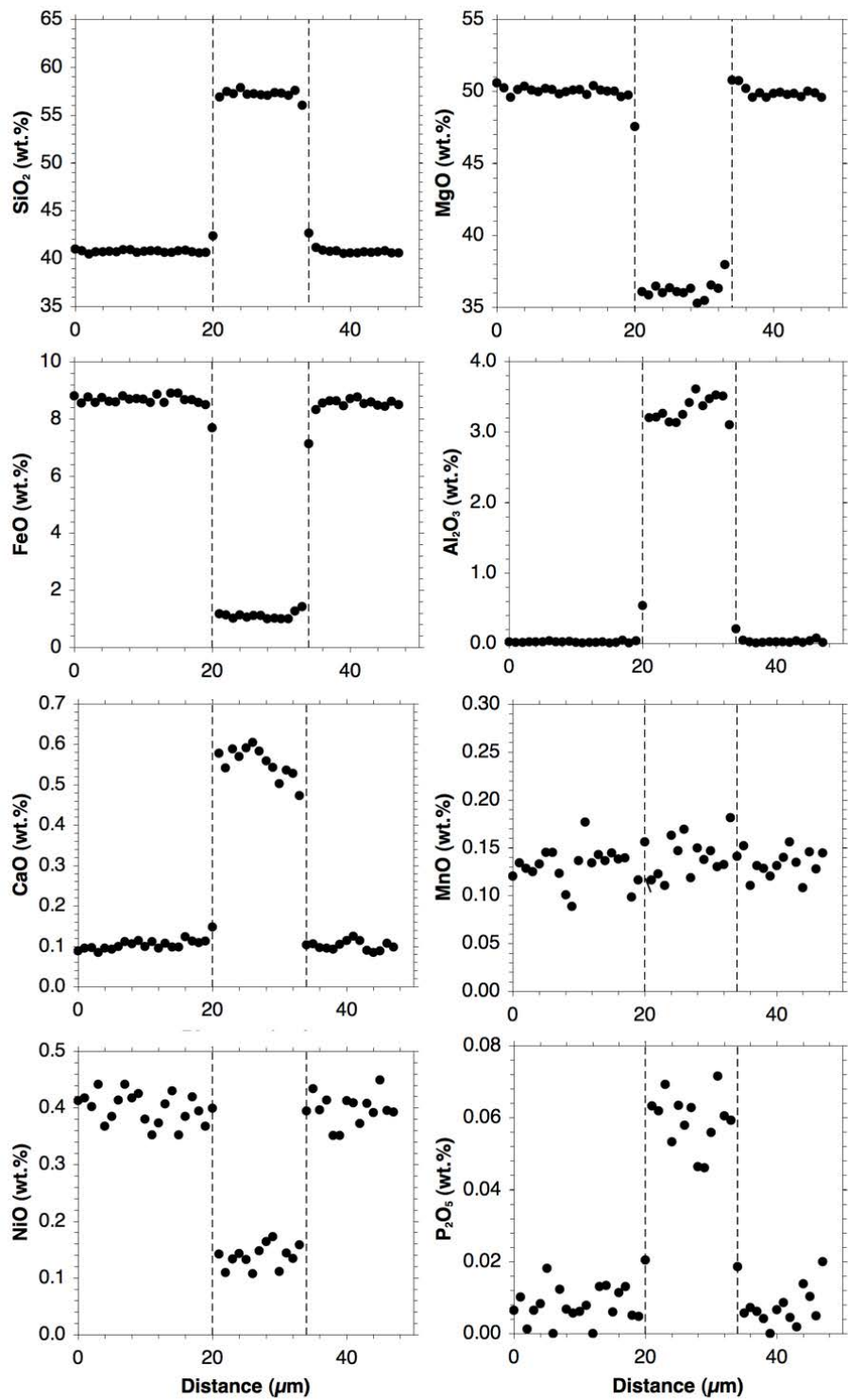


Figure 6.

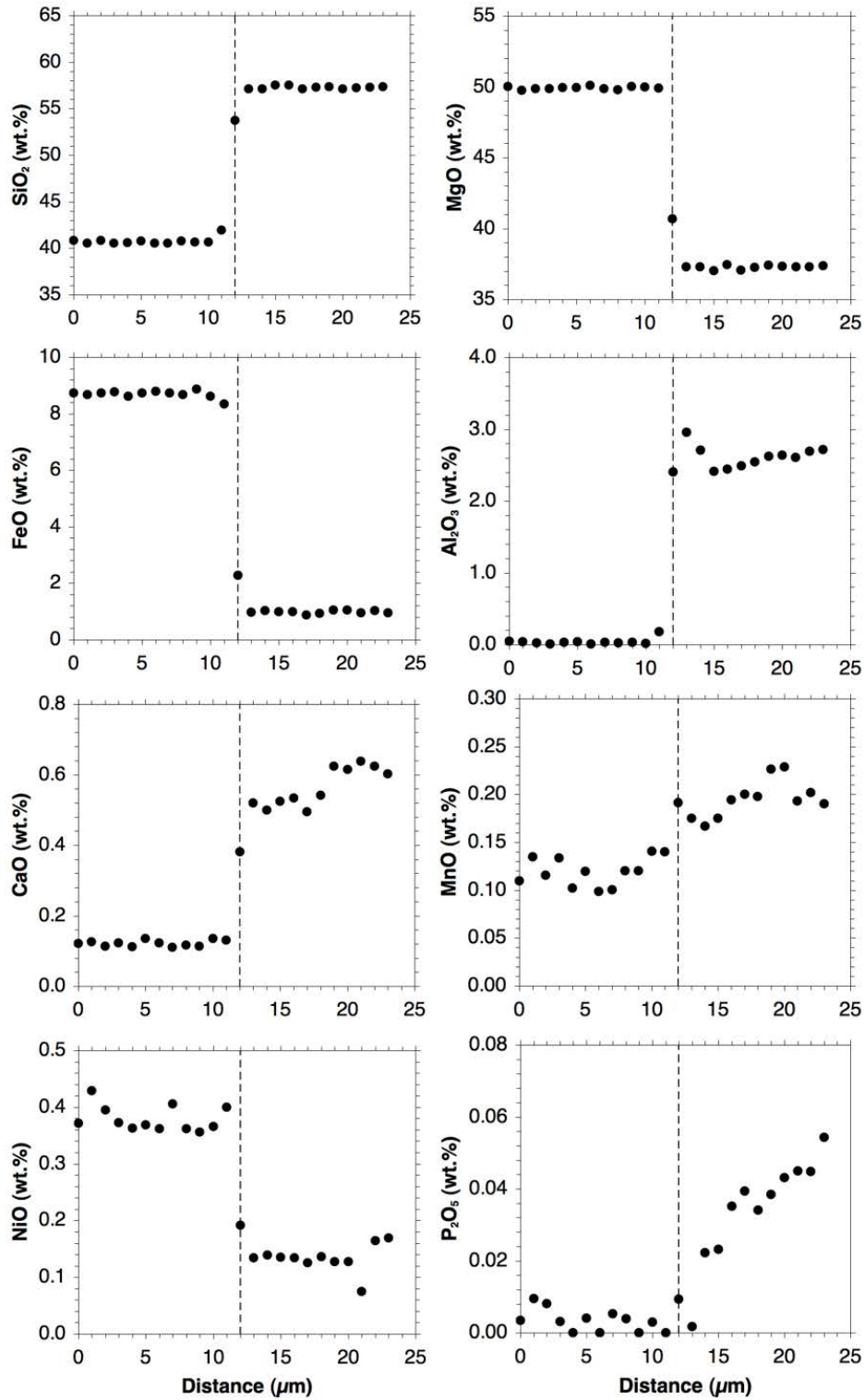
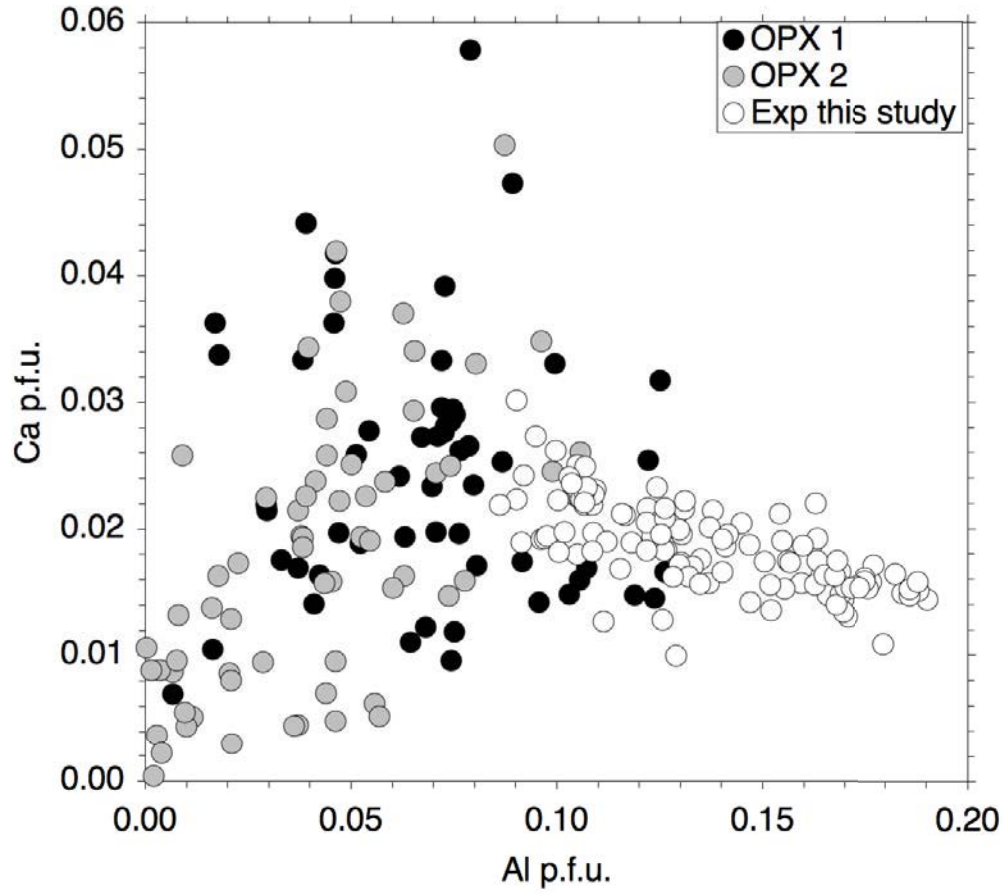
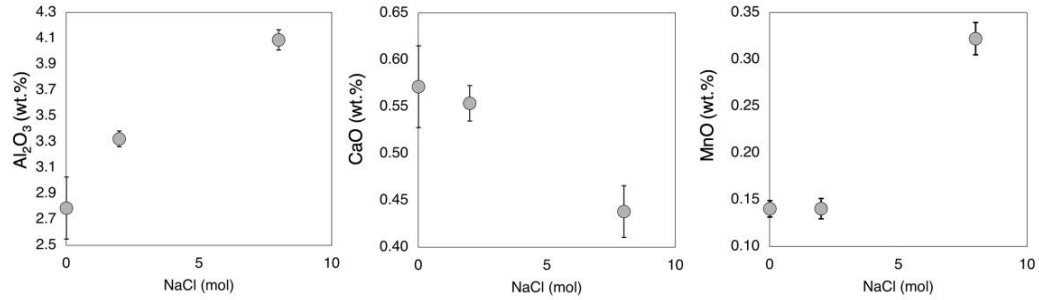


Figure 7.



**Figure 8.**



**Figure 9.**

